Global NEST Journal, Vol 26, No 7, 06252

Exploring the effective industrial dye pollutants degradation mechanism of MgO-rGO nanocomposites under sunlight as a sustainable and economical wastewater treatment solutions

Veera Prabakaran Elanjeitsenni* and Senthil Vadivu Kulandhaivelu
Department of Printing and Packaging Technology, College of Engineering Guindy, Anna University, Chennai, 600025, Tamil Nadu, India.
Received: 11/06/2024, Accepted: 11/07/2024, Available online: 12/07/2024
*to whom all correspondence should be addressed: e-mail: veeraprabakaranprintpack@gmail.com
https://doi.org/10.30955/gnj.06252

Graphical abstract

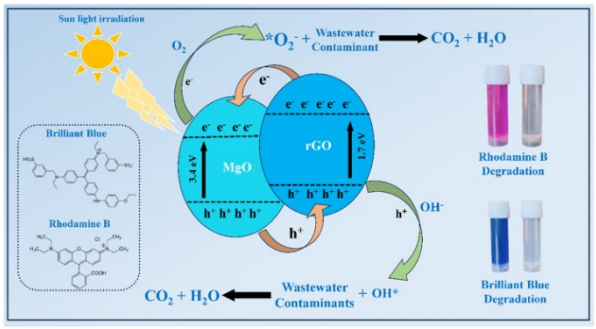

Abstract

The increasing prevalence of hazardous dye wastewater from the printing and packaging industries poses significant environmental and health challenges. Conventional water treatment technologies often fall short of effectively removing these complex contaminants. This study explores the formulation of magnesium oxide (MgO) nanoparticles using *Helianthus annuus* (sunflower) leaf extracts and their integration with reduced graphene oxide (rGO) to form MgO-rGO nanocomposites. The biosynthesis method employed is cost-effective and environmentally friendly. The synthesized nanocomposites were characterized for their physicochemical properties, including structural, morphological, and optical characteristics. The photocatalytic commotion of these nanocomposites was assessed through the deprivation of cationic Rhodamine B and anionic Brilliant Blue dyes under sunlight irradiation. The results highlight the potential of MgO-rGO nanocomposites as effective photocatalysts for industrial wastewater treatment, exhibits an effectual resolution for the printing and packaging industry.

Keywords: Photocatalytic activity, wastewater treatment, Helianthus annuus, MgO, reduced graphene oxide.

1. Introduction

The composition of contaminants observed in industrial wastewater varies depending on the factory and industry. The printing and packaging sector has played a significant part in generating industrial wastewater pollution. The industry uses various techniques, including printing, coating, laminating, and finishing, which include diverse chemicals such as dyes, inks, solvents, adhesives, and varnishes (Sharmin *et al.* 2021). The increasing proliferation of hazardous dye wastewater produced by different industries remains an urgent public health problem and a substantial environmental concern, presenting a notable barrier to current conventional water treatment facilities. The textile industry, recognized as a significant sector in the world economy, faces substantial environmental issues. The textile industry has several challenges related to chemical processes, ranging from early sizing to final washing, which occurs in severe environments (Zhou *et al.* 2011). The paper and packaging sector mainly releases suspended particles and high organic compounds, the primary water pollutants. The effluent quality varies depending on the grade of the paper generated and the processing methods used. The effluent generated by these procedures has elevated concentrations of pollutants that may provide significant environmental and health hazards if not adequately treated before being released into aquatic ecosystems (Meher-Un-Nisa *et al.* 2023).

The increasing production of hazardous dye wastewater by various industries is a critical public health problem and a huge environmental issue, presenting a substantial obstacle to current conventional water treatment technologies. The printing and dyeing wastewater contains a complex mixture of dyes with high concentrations and intense colors. It also contains numerous substances that are difficult to biodegrade and various organics that possess biological toxicity such as humic acids, microplastics, fulvic acids, tannins. Consequently, achieving the desired treatment outcome using a single technology is often challenging. In addition

to their vibrant color, these wastewaters exhibit high levels of chemical oxygen demand (COD), usually reaching up to 20,000 mg/L (Lin *et al.* 2023). Hence, exposing printing ink effluent to treatment before releasing it is crucial to avoid severe environmental issues. The substance contains high concentrations of heavy metals such as lead, cadmium, and chromium, as well as poisonous organic chemicals that may harm aquatic organisms. The chemicals used for cleaning printing equipment might add to the accumulated chemical strain in effluent (Kannan *et al.* 2024). The presence of many pollutants complicates the treatment procedure. Much research has been conducted to detoxify the environment from dangerous contaminants by creating various nanoscale materials. Conventional treatment procedures may not effectively remove all sorts of pollutants found in wastewater. Small to medium-sized firms generally face challenges in implementing advanced treatment technologies due to the high costs associated with handling complex mixtures of contaminants. The industry must seek sustainable and economical approaches to wastewater treatment that minimize chemical treatments, which could result in additional pollutants (Kant *et al.* 2022). Utilizing methods such as photocatalysis degrade organic pollutants into less harmful substances. Unlike other treatment methods that only transfer contaminants from one phase to another, photocatalysis can completely mineralize organic dyes into harmless end products. Photocatalysis is a promising method for removing and degrading organic dyes from wastewater. This technique utilizes light energy, typically UV or visible light, to activate a photocatalyst, which then induces a series of chemical reactions that degrade organic pollutants into less harmful substances. The mercurial oxygen types generated in the photocatalytic progression are highly reactive and can oxidize organic dye molecules, breaking them down into more minor, less harmful compounds, ultimately leading to complete mineralization into inorganic ions, CO_2, and H_2O. *Helianthus annuus*, commonly known as sunflower, is increasingly used in the green formulation of metal-oxide NPs (Shuai *et al.* 2020). The plant extracts encompass several bioactive complexes that act as alleviating, plummeting, and capping representatives throughout synthesis. This method is cost-effective, eco-friendly, and sustainable compared to conventional chemical and physical processes. Several quantified photocatalysts have been widely used. Metal oxide nanoparticles synthesized using *Helianthus annuus* extracts display high catalytic commotion due to their huge surface area and the existence of bioactive complexes. The MgO is a highly reactive substance with a notable ability to absorb substances and is quickly produced. Recently, it has been utilized in various applications, such as catalysis, ceramics, sewage handling, antiseptic complexes, and other sectors. Nevertheless, because of its significant bandgap energy and rapid charge transporter recombination, pure MgO exhibits minimal change in photocatalytic activity (Arshad *et al.* 2017).

Graphene, a 2D network of hexagonally systematized sp_2-hybridized carbon molecules, has recently attracted considerable academic attention in energy adaption and photocatalysis. Graphene has two oxidative derivatives: GO and reduced rGO. When used as a supporting material in forming a composite containing photocatalysts, rGO exhibits superior photocatalytic activity compared to GO. Thus, our work examines the currently available printing and packing industry wastewater treatment technologies. We synthesized MgO nanoparticles using *Helianthus annuus* leaf extracts, and rGO was prepared using the modified hummers method, while the MgO doped rGO nanocomposite was prepared using a simple reflux method. The physiochemical, optical, and structural morphology have been analyzed. Additionally, applications such as electrochemical studies (EIS and Bode plot) and photocatalytic activity using cationic (Rhodamine B) and anionic (Brilliant Blue) dyes were examined under sunlight irradiation (Zen *et al.* 2021).

2. Experimental procedure

2.1. Chemicals and reagents used

The *Helianthus annuus* (Sunflower) Leaves were used to prepare the plant extract—magnesium chloride ($MgCl_2$) precursor. The GO, concentrated H_2SO_4, Sodium nitrate ($NaNO_3$), and potassium permanganate ($KMnO_4$) is used as an oxidizing agent for graphite. Hydrogen Peroxide (H_2O_2) stops the reaction and reduces the residual manganese compounds. Hydrochloric Acid (HCl) is used to wash the GO. Deionized water is used throughout the synthesis and washing processes.

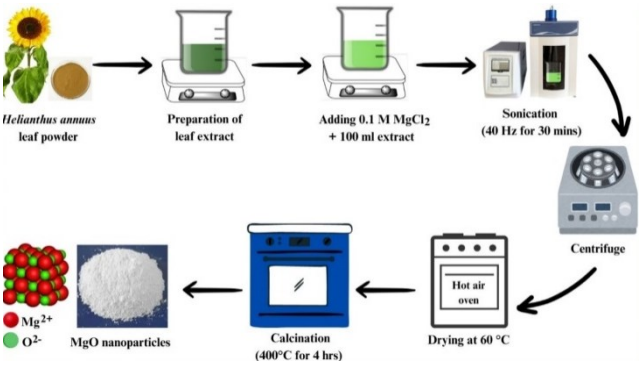

Figure 1. Pictorial representation of nanoparticle synthesis

2.2. MgO nanoparticle synthesis

Double-distilled water was used to completely rinse fresh Helianthus annuus leaves to eliminate the dust particles, and then the leaves were allowed to air dry for two days. Using a home mixer, the leaves that had been shade-dried were ground into fine powder. Further, 30 g of finely powdered leaves were added with 150 mL of deionized water and enthused at 80^0C for 24 hours. Afterward, the solution was cooled at ambient temperature. Further, using a suction pump, the extract was extracted using Whatman's No. 1 filter paper. A stoichiometric amount of 0.1 M (2.05 g) $MgCl_2$ was added as a precursor to 100 mL of leaf extract with constant stirring at room temperature. The solution was then still left for 24 hours for the aging process. Later, it was sonicated for 30 min to prevent agglomeration of particles and breakdown of chloride

precursor. Then, it was centrifuged at 5000 rpm for 10 min with ethanol and deionized water several times. Ethanol was employed in centrifuge washing to eliminate residual particles aggregated with the sample since it has a more significant vapor pressure than water. Then, it was later desiccated using a hot-air oven at 60^{0}C. Further, the dried sample was calcinated at 400°C for 4 hours using a muffle furnace (Yousefi *et al.* 2018). Finally, green synthesized MgO nanoparticles have been obtained. The pictorial representation of the synthesized nanoparticle is presented in Figure 1.

2.3. Synthesis of GO

The Hummers' method is widely used to oxidize graphite and produce graphene oxide, a precursor for various graphene-based materials. Initially, 3g of graphite flakes were added to the 150 ml conc. H_2SO_4 and 3g of $NaNO_3$ are added gradually to dissolve completely. Adding $NaNO_3$ oxidizes the graphite and stirs the mixture for 12 hours. After 12 hours, 18 g of KMnO4 is added for further oxidation, penetrating the graphite layers and stirring until it becomes thick. The addition of $KMnO_4$ should be conducted in an ice bath, which releases an excess amount of heat. So, the process should be conducted in an ice bath. The thick slurry layer indicates that the graphite gets expanded, and there is breakage of Vander Waals force. Then 200 ml of distilled water is added to reduce its thickness, and 30 ml of H_2O_2 is added to terminate the reaction. The H_2O_2 minimizes the amount of $KMnO_4$ added. Finally, 10% of HCl is added and centrifuged to remove the various metals and contaminants in the graphene oxide solution. The centrifugation should be done until it attains neutral pH (Guo *et al.* 2021). The flow chart for the graphene oxide synthesis using Modified Hummer's method is presented in Figure 2.

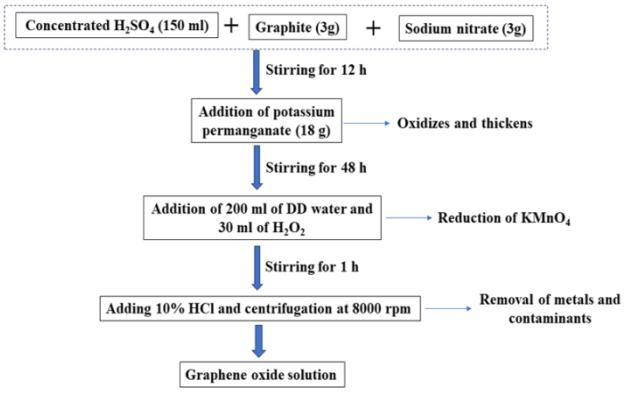

Figure 2. Modified Hummer's method

2.4. Formulation of MgO doped rGO nanocomposites

To prepare the MgO-rGO nanocomposites, an equal ratio of prepared MgO NPs and rGO were dispersed in 200 mL of DD water and continuously stirred for 40 min. Then, the mixture is transferred in a reflux setup for 8 hours at 80 °C. Later, the solution is set aside at room temperature for 24 hrs and dried in a hot-air oven at 70°C. After drying, it was calcinated at 200°C for an hour (Mohamed *et al.* 2024). The calcinated sample was named MgO-rGO nanocomposite. The schematic representation is presented in Figure 3.

2.5. Photocatalytic degradation activity

The synthesized MgO nanoparticles and MgO and rGO nanocomposite demonstrated photocatalytic activity by degrading cationic Rhodamine B dye and anionic Brilliant Blue dye when exposed to sunlight irradiation. An initial dye concentration was first optimized for maximal degradation efficiency within a constrained time. Subsequently, at room temperature, 0.5 g/L of nano-catalyst and five mg/L of dyes were added to prepare the experimental nano-suspension solution. The concoction was agitated in darkness for 30 min to achieve equipoise before being exposed to sunlight. After every 15 minutes of irradiation, 5 ml of the solution combination was taken out and analyzed using UV-Vis spectroscopy to assess the dye degradation. The treatment was maintained until the dye molecules were utterly degraded. The equation (1) below can determine the degradation efficiency using a nano-catalyst (Nagi *et al.* 2021).

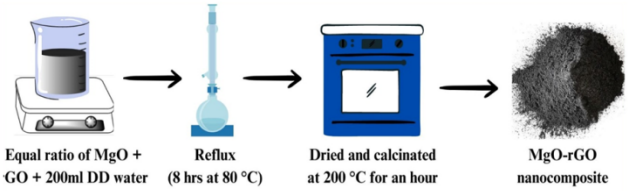

Figure 3. Schematic representation of prepared nanocomposite

$$\text{Degradation efficiency}(\%) = \frac{1\text{-Ct}}{\text{Co}} \times 100 \quad (1)$$

Here, Co and Ct are the initial and final concentrations of pharmaceutical pollutants.

2.6. Electrode preparation for electrochemical analysis

A 1 cm^2 MS plate served as the dynamic material in the study of the charge transfer characteristics. The MS plate was cleaned thoroughly with acetone and polished using silicon carbide (SiC) grid paper. Next, 15 mg of synthesized nanoparticles were combined with 4 mg of polyvinylidene fluoride and 7 mL of N-Methyl-2-pyrrolidone to create a homogeneous slurry. The doctor blade method coats the slurry on the MS plate.

2.7. Characterization techniques

The FTIR spectroscopy was performed on the prepared samples to identify surface functional groups and XRD is used to analyze the crystallite size, crystallinity and phase determination of the synthesized materials. The UV-Vis analysis was performed at 200-800 nm wavelength to study optical properties and observe dye degradation. The surface syllable structure was examined through FE-SEM analysis and EDX was used to govern the elemental composition. The EIS experiment was conducted using NaCl electrolyte and a three-electrode setup, utilizing an electrochemical workstation at chamber temperature.

3. Results and Discussion

The XRD analysis was conducted to determine the crystalline structure, phase composition, and structural

parameters of prepared MgO nanoparticles and MgO-rGO nanocomposite, and the XRD spectra are shown in Figure 4. The 2θ position of pure MgO powder is noted at 37.4°, 43.3°, 62.9°, 75.6°, 79.3°. The obtained 2θ values correspond to specific crystal planes in the MgO cubic crystal structure (JCPDS No. 87-0653) with corresponding miller indices planes of (111), (200), (220), (311), and (222), correspondingly (Ahmad *et al.* 2023). The peaks specify the presence of MgO with a high degree of crystallinity. The peak at 43.3° is one of the most intense peaks for cubic MgO, confirming the dominant cubic phase of the nanoparticles. The bioactive compounds in the extract facilitate the formation of crystalline MgO nanoparticles. Further, the absence of additional peaks suggests that the MgO is phase-pure without significant impurities.

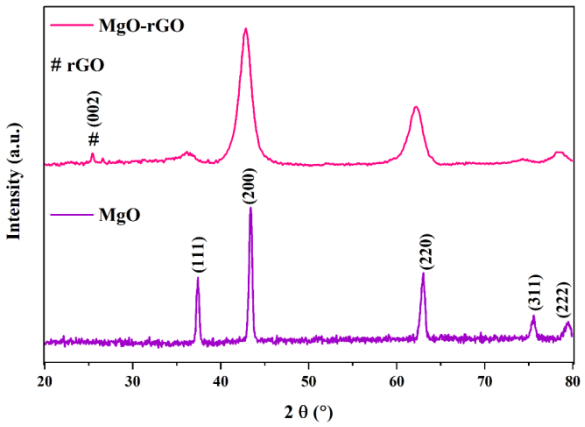

Figure 4. XRD spectra for synthesized rGO and MgO

The incorporation of rGO into the MgO matrix influences the diffraction pattern. The characteristic peaks of MgO doped rGO were noticed at angles (2θ) of 25.4°, 36.2°, 42.9°, 62.3°, 74.2°, and 78.5° respectively are shifted compared to pure MgO, indicating interactions between MgO nanoparticles and rGO sheets. The peak at 25.4° is the characteristic of rGO, corresponding to the (002) plane of reduced graphene oxide. It indicates the presence of graphene layers within the composite (Asgari *et al.* 2020). The presence of organic molecules in the extract on the surface of MgO nanoparticles can cause slight lattice distortions. These distortions might lead to minor shifts in the peak positions in the XRD pattern. The change and potential broadening of MgO peaks suggest that the rGO incorporation causes lattice distortions and possibly reduces the crystallite size of MgO. The crystallite magnitude of the synthesized NPs and nanocomposite is estimated using the Scherrer equation. Thus, it exhibits approximately 21 and 14 nm crystalline sizes, respectively. It was found that the green extract effectively reduced chloride precursors during synthesis, as evidenced by the observed crystalline phase and size.

3.1. Functional characteristic analysis

The FTIR was analyzed to recognize the functional clusters of prepared nanoparticles and composite, and the FTIR spectrum peaks correspond to the vibrational frequencies of the bonds in the molecules, as shown in Figure 5. The FTIR spectra of MgO and MgO-rGO nanopowder are recorded in the 400-4000 cm-1 range. The crests at 555 and 432 cm^{-1} are due to the stretch and bending vibrations of the Mg-O bond. The peaks observed in the MgO-rGO nanocomposite also correspond to the Mg-O bond vibrations but with slight shifts due to the interaction with rGO. The IR characteristic of rGO in MgO nanopowder at 1220 to 1050 cm^{-1} stretching vibrations represents C-O epoxy and hydroxyl groups (Yadav *et al.* 2023).

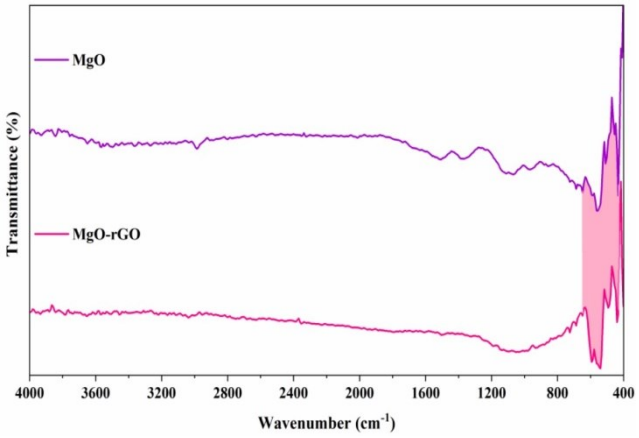

Figure 5. Functional groups analysis for the prepared nanopowder

The presence of rGO can cause slight changes in the Mg-O bonds, leading to these shifts in vibrational frequencies. The FTIR spectra for MgO show only peaks corresponding to Mg-O bonds, indicating high purity with no significant contamination. The peaks observed in the FTIR spectrum are due to the vibrations of the Mg-O bonds (Zheng *et al.* 2019). The bioactive compounds in the extract do not introduce significant additional functional groups detectable in the FTIR spectrum, indicating effective capping and stabilization without altering the MgO.

3.2. Morphology

The Figure 6 displays the surface morphology of the produced MgO nanoparticle and the MgO-rGO composite. The acquired FE-SEM images depict the formation of micron-sized particles that exhibit a spherical and irregular morphology with an agglomeration. Agglomeration demonstrates a notable interaction among the NPs and significant surface-free energy. The phytochemical components found in extracts functioned as surfactants, substantially decreasing the size and affecting the silhouette of produced MgO NPs. Additionally, the picture of the nanocomposite reveals the existence of fine MgO nanoparticles inside the rGO structure. The morphology of rGO appears to have a sheet-like structure consisting of a few layers of carbon sheets. The aggregation of the reduced GO layers is caused by the abolition of oxygen-containing compounds during the reduction process of GO. The EDAX elemental mapping of MgO and MgO-rGO nanopowder (Figure 6 (b)(d)) displays the peak intensity with quantitative measurements. The composition of the substance consists of about 55.65 wt.% magnesium and 44.35 wt.% oxygen. Based on the composition, the sample appears predominantly made up of magnesium and oxygen atoms

(Wu *et al.* 2018). The high magnesium concentration suggests that the synthesis technique effectively produced a sample with significant MgO.

For the prepared MgO-rGO composite, the nanopowder consists of Mg, O, and residues of carbon (C) elements, confirming that there were no other additional impurities. However, the presence of carbon (C) element might be attributed to the accumulation of phytochemicals on the nanoparticles surface. The elemental composition of the nanocomposite is significantly revealed by the EDAX analysis, which also ensures that different elements are included in the prepared sample (Gusain *et al.* 2019). Figure 7 shows the elemental imaging of the MgO-rGO nanocomposite. It reveals the uniform distribution of each component of the MgO-rGO nanocomposites.

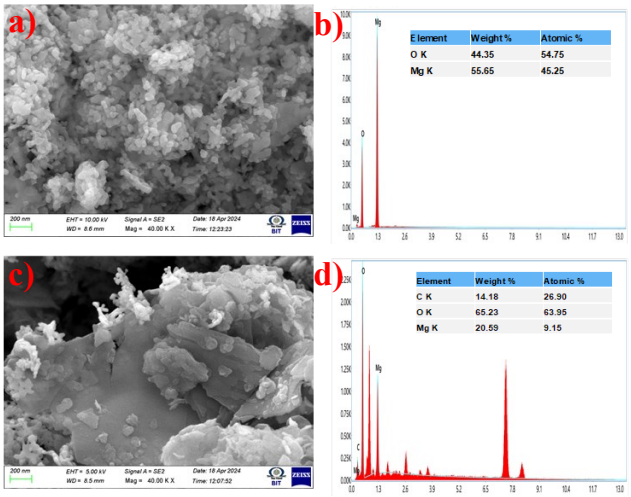

Figure 6. a) and c) FESEM analysis for prepared MgO nanoparticle and composite. b) and d) EDX analysis for nanoparticle and composite

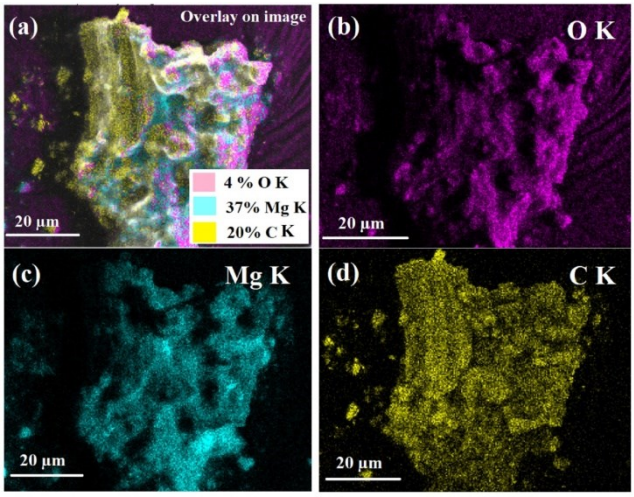

Figure 7. Mapping images of MgO-rGO nanocomposite

3.3. Particle size

To assess the average size of the particles in the formulated sample, particle size analysis was analyzed and shown in Figure 8. MgO Nanoparticles exhibit smaller particle size with d50=14.35 nm. The bioactive compounds in the extract effectually act as a capping agent with the MgO nanoparticles, preventing excessive growth and agglomeration. This results in a smaller and more uniform particle size. For MgO-rGO nanocomposite, a larger particle size of d50 = 21.5 nm is observed. The rise in particle size can be attributed to the interface amongst MgO nanoparticles and rGO sheets. The presence of rGO can lead to a more extensive network structure, causing the particles to appear larger in size analysis. Thus, rGO plays a noteworthy part in influencing the structure and size distribution of the nanocomposite material. Further, this increase in particle size may lead to a decreased surface area, which could enhance the catalytic properties of the MgO-rGO nanocomposite.

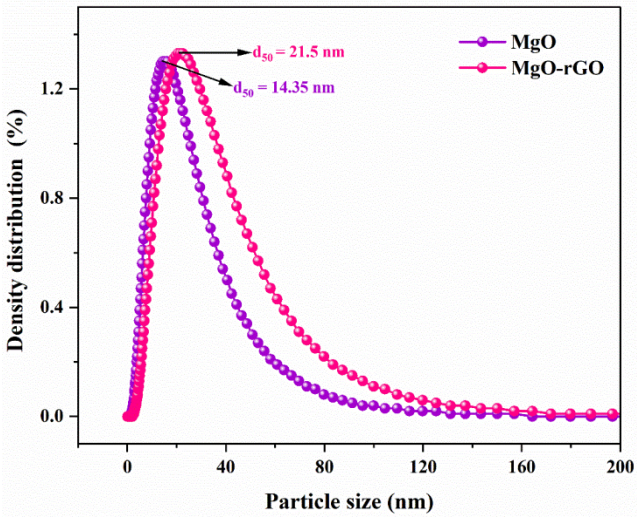

Figure 8. PSA image for the prepared nanoparticle and composite

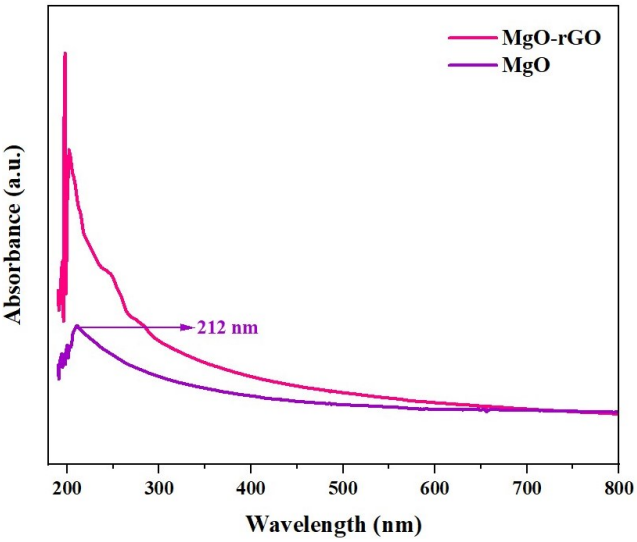

Figure 9. Optical property of prepared nanoparticle and composite

The electronic transitions and the bandgap of the prepared MgO nanoparticle and MgO-rGO composite are analyzed using UV-visible spectroscopy and depicted in Figure 9. The MgO nanoparticles show an absorbance peak at 212 nm, while the MgO-rGO composite peaks at 201 nm respectively. Incorporating rGO into the composite can lead to interactions between the MgO nanoparticles and the rGO sheets. These interactions can alter the electronic edifice of the MgO nanoparticles, force to a shift in the absorption peak. The existence of rGO might further reduce the adequate particle size of MgO due to better dispersion and prevention of

agglomeration. This can enhance the quantum confinement consequence, resulting in a further blue shift of the absorption peak, which correlates with increased bandgap energy. The absorption spectra determine the direct bandgap for nanoparticles and composite through Tauc's plot. The absorption coefficient can be determined by relating it to the energy of the incident photons through the succeeding equivalence (2) (Nagi et al. 2021).

$$\alpha(\upsilon)\mathrm{h} = \mathrm{K}(\mathrm{hv} - \mathrm{Eg})^{n} \quad (2)$$

Where α is the absorption coefficient, which measures the light of a particular wavelength absorbed by the material, hv represents the photon energy, where h is Planck's persistent and v frequency of the occurrence light. K is a proportionality persistent that depends on the material. For example, it represents the material's optical band gap energy, while the electronic transition's nature determines the proponent n. The direct allowed transitions occur when n=1/2, while ancillary allowed changeovers occur when n=2. Based on the calculations, the bandgap for MgO and MgO-rGO is 3.46 and 3.1 eV, respectively. This suggests that these materials are ideally suited for photocatalytic activity. rGO can interact electronically with metal oxide nanoparticles. This interaction can alter the electronic edifice of the metal oxide, force to an increase in bandgap.

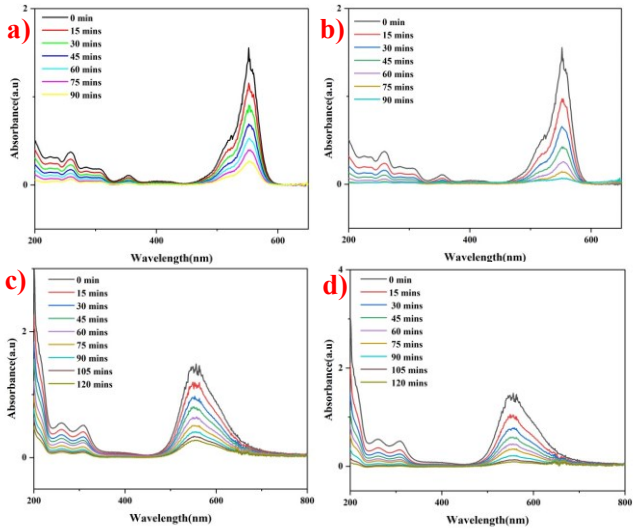

Figure 10. Absorbance-dye degradation graph of cationic dyes: a) MgO, b) MgO-rGO; Anionic dyes: c) MgO, d) MgO-rGO

The photocatalytic capacities of the prepared nanopowder and nanocomposite were examined by subjecting them to visible-light irradiation and observing their ability to degrade representative organic dyes, namely a cationic dye (rhodamine B) and an anionic dye (Brilliant Blue). Observing the changes in the intensity of the absorption peak through optical absorption spectroscopy allows for easy monitoring of its degradation as the absorption peak falls within the visible range. As the radiation time increases, the UV-Vis spectroscopy results show a gradual decrease in the optical absorption levels of rhodamine B and Brilliant blue dye. This indicates that the catalytic reaction of MgO nanoparticles and MgO-rGO composites effectively breaks down the dye molecules, as shown in Figures 10 and 11 shows the photocatalytic dilapidation mechanism of the prepared MgO and MgO-rGO nanocomposite under sunlight irradiation. Figure 10 illustrates the changes in photocatalytic activity over time for the synthesized nanoparticle and nanocomposite. The degradation of Rh B and BB dyes was measured at 15-minute intervals, with a maximum irradiation time of 90 and 120 minutes, respectively. When the irradiation time is extended, the vigorous absorption/peak intensity of nanocatalyst-suspended dye solutions gradually decreases after irradiation. Additionally, the nano-catalyst plays a role in the gradual decolorization of both RhB and BB dye solutions, which also varies with irradiation. After irradiation, the maximum degradation of RhB dye efficiency is 94.9 and 95.39 %, respectively, for MgO nanoparticle and MgO-rGO composites, as shown in Figure 12. Similarly, the maximum degradation of BB dye is 82.07 and 94.06 %, respectively. Furthermore, it is notable that the degradation efficiency for RhB and BB dye without nano-catalyst is 1.92% and 2.69%, respectively. MgO is a wide-bandgap semiconductor, primarily absorbing UV light. The MgO-rGO composite can absorb a broader spectrum of sunlight due to the synergistic effect of rGO (equations 3 and 4). Upon absorption of UV light, the nano-catalyst generates electron-hole pairs (Meher-Un-Nisa et al. 2023).

$$MgO + hv \rightarrow \mathrm{MgO}(\mathrm{e}- + \mathrm{h}+) \quad (3)$$

$$MgO - rGO + hv \rightarrow \mathrm{MgO}(\mathrm{e}\mp\mathrm{h}+) + rGO \quad (4)$$

The generated electron-hole pairs can quickly recombine, reducing photocatalysis's efficiency. rGO acts as an electron acceptor, facilitating charge separation by transferring electrons from MgO to rGO (Equation 5). This reduces the recombination of electron-hole pairs (Sharmin *et al.* 2021).

$$MgO(e- + h+) \rightarrow \mathrm{MgO}(\mathrm{h}+) + rGO(e-) \quad (5)$$

The valence band of MgO contains holes (h^+) that can oxidize water or hydroxide ions, producing hydroxyl radicals and electrons (e^-) in the conduction band (Equations 6-8). These electrons may then reduce oxygen molecules to form superoxide radicals (Wang *et al.* 2020).

$$h^+ + H_2O \rightarrow H^+ + OH^* \quad (6)$$

$$e^- + O_2 \rightarrow O_2^{-*} \quad (7)$$

$$\text{Dye molecules} + {}^{*}\mathrm{HO} + \mathrm{O}_{2^-} \rightarrow \text{Degraded products}(\mathrm{CO}_2 + \mathrm{H}_2\mathrm{O}) \quad (8)$$

The generated hydroxyl radicals (·OH) and superoxide radicals ($\cdot O_2$) are highly reactive and can attack dye molecules, breaking them down into less harmful compounds. The complete possible photocatalytic degradation of the prepared nanocomposite is shown in Figure 11.

The results indicate that RhB, being positively charged, readily adsorbs onto the negatively charged sites on the MgO surface. This strong electrostatic attraction facilitates close interaction between the dye particles and the reactive sites of the photocatalyst. Once adsorbed, the mercurial oxygen types engendered on the MgO-rGO can effectively interact with and degrade Rhodamine B molecules. The high adsorption efficiency and effective charge separation lead to rapid and high-efficiency degradation. Thus, the strong electrostatic lure amongst the absolutely stimulating RhB and depressingly charged sites on MgO enhances adsorption, facilitates rapid degradation by reactive species, and results in high degradation efficiency (95.93%) within a shorter irradiation time (90 mins).

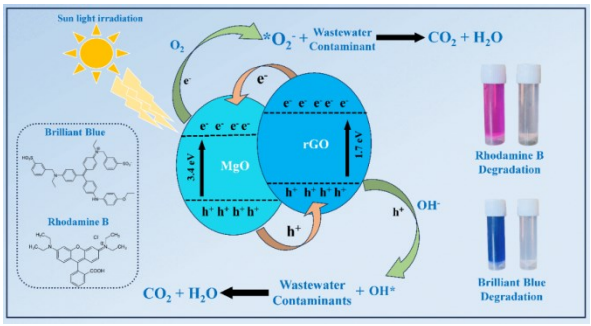

Figure 11. Probable photocatalytic degradation mechanism

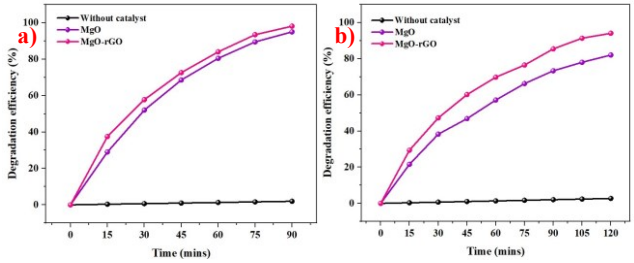

Figure 12. Degradation efficiencies against cationic dyes: a) MgO, b) MgO-rGO; Anionic dyes: c) MgO, d) MgO-rGO

Table 1. Nano-catalyst with Degradation Rate Constant and its Efficiency

Samples	Dye	Kinetic rate constant (× 10^{-2} min^{-1})	Dye degradation efficiency (%)
MgO	Rh B	3.26	94.9
	BB	1.42	82.07
MgO-rGO	Rh B	3.33	95.39
	BB	2.29	94.06

The BB dye, being negatively charged, interacts differently with the photocatalyst. It may adsorb onto neutral or positively charged sites on the MgO surface. The interaction might be less intense than the cationic dye, resulting in slightly slower degradation kinetics. Despite the weaker adsorption, the volatile oxygen species produced on the MgO-rGO can still effectively degrade BB dye molecules. The presence of rGO ensures efficient charge separation and a sustained generation of reactive species, contributing to high overall degradation efficiency. Thus, the interaction between negatively charged BB dye and the photocatalyst is weaker than RhB. This results in slightly slower adsorption and degradation kinetics, and results with high degradation efficiency (94.06%) are still achieved but require a longer irradiation time (120 mins) to reach similar levels of degradation. The degrading effectiveness, rate constant, and linear regression of the MgO and MgO-rGO nanocomposite are revealed in Table 1.

Figure 13 displays the pseudo-first-order kinetic reaction and C/Co values for degrading RhB and BB dyes using MgO NPs and MgO-rGO composites under UV irradiation. The response magnitude is increased as C/Co, where Co represents the starting magnitude, and C represents the concentration of RhB and BB dye subsequently the dilapidation period, as seen in Figure 13 which shows the dynamic deprivation rate and is determined using the following Equation 9 (Kannan *et al.* 2024).

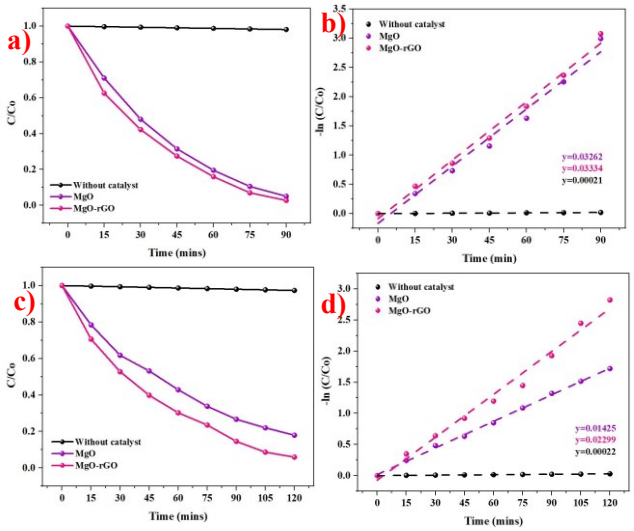

Figure 13. C/Co curves and degradation kinetics: a) MgO, b) MgO-rGO; Anionic dyes: c) MgO, d) MgO-rGO

$$Kt = \ln\left(\frac{C}{CO}\right) \quad (9)$$

Where, t is the time, k is the rate constant, and C_o and C_t are the dye concentrations before and following. Reaction rate constants for RhB dye are estimated as 0.00021, 3.26, and 3.33 X 10^{-2} min^{-1} for without catalyst, MgO, and MgO-rGO composite, respectively. Similarly, BB dye is assessed as 0.00027, 1.42, and 2.29 X 10^{-2} min^{-1} without catalyst, MgO, and MgO-rGO composite, respectively. RhB dye exhibits higher degradation efficiency and kinetic rate constant than BB dye. The presence of phytochemicals may also improve the generation of ROS (*OH and $*O_2$–), which are vital in degrading dye molecules. Moreover, rGO acts as an excellent electron acceptor, reducing electron-hole recombination and allowing more reactive species to form. Thus, it concludes that MgO provides vigorous photocatalytic activity, while rGO enhances charge separation and extends light absorption slightly into the visible range.

Electrochemical impedance spectroscopy (EIS) investigated the resistance to charge transfer and separation effectiveness between photogenerated electrons and holes in MgO nanoparticles and MgO-rGO nanocomposites. This investigation aimed to assess the impact of charge separation efficiency on photocatalytic

activity, as it is a crucial factor. Figure 14 displays standard EIS Nyquist plots of MgO NPs and MgO-rGO nanocomposites when exposed to visible light. The EIS spectra's arc radius measures the resistance exhibited by the interface layer that develops on the electrode's surface. A smaller arc radius is associated with a greater charge transfer efficiency. The arc radius of the MgO-rGO nanocomposite was less than that of MgO NPs. These findings indicate that the MgO-rGO nanocomposite photocatalysts exhibit reduced resistance compared to the MgO nanoparticle photocatalyst, resulting in an enhanced interfacial charge-transfer mechanism. These discoveries corroborate the conclusions of the UV-Vis band and the results of the photocatalytic degradation generated by sunlight. EIS further confirmed the significant contribution of rGO and various forms of oxygen vacancies and defects. These factors enhance the efficiency of charge separation and transfer of the electrons and holes created by light on the surface of the MgO-rGO photocatalysts. The outcomes from the EIS investigation validate the findings from the photodegradation experiments. The MgO-rGO nanocomposite photocatalyst demonstrated superior degradation efficiency compared to MgO NPs in the experiments. This can be attributed to the catalyst's enhanced charge separation efficiency, which consequently increased its photodegradation activity. These data validate the correlation between semiconductors' crystallinity and electrochemical and photocatalytic activity. Using MgO-rGO nanocomposites signifies a significant advancement in industrial wastewater treatment, offering the printing and packaging industry an effective, sustainable, and economical solution to manage dye wastewater pollution.

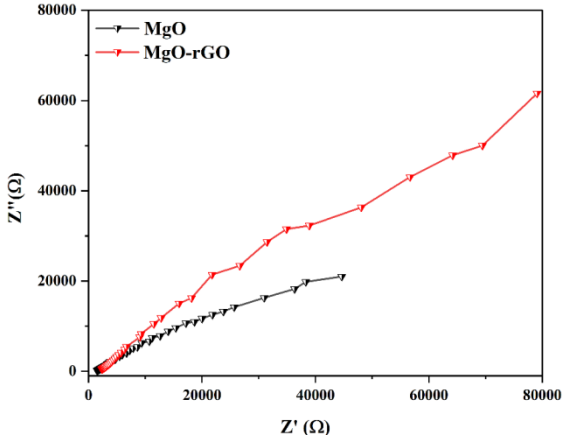

Figure 14. EIS plot (Nyquist plot) of MgO and MgO-rGO nanocomposites

4. Conclusion

The biosynthesis of MgO nanoparticles using *Helianthus annuus* leaf extracts and their subsequent incorporation into rGO to form MgO-rGO nanocomposites presents a promising approach for industrial wastewater treatment. The study confirms the high photocatalytic efficiency of these nanocomposites in degrading complex dye pollutants under sunlight, making them suitable for sustainable and economical wastewater treatment solutions. The synthesized MgO nanoparticles showed an average size of 14.35 nm, while the MgO-rGO nanocomposites showed a slightly larger size of 21.5 nm. The XRD analysis confirmed the successful incorporation of rGO, with characteristic peaks indicating interactions between MgO and rGO. FTIR analysis revealed functional groups corresponding to Mg-O and rGO interactions, while SEM images showed well-dispersed nanoparticles within the rGO matrix. The degradation efficiency of the dyes exceeded 90% under sunlight irradiation, showcasing the composite's high photocatalytic activity.

References

Ahmad A, Khan M, Khan S. Bio-construction of MgO nanoparticles using Texas sage plant extract for catalytical degradation of methylene blue via photocatalysis. (2023). *International Journal of Environmental Science and Technology*, **20**, 1451–1462,

Arshad A, Iqbal J, Siddiq M, Mansoor Q, Ismail M, Mehmood F, Ajmal M, Abid Z. (2017). Graphene nanoplatelets induced tailoring in photocatalytic activity and antibacterial characteristics of MgO/graphene nanoplatelets nanocomposites. *Journal of Applied Physics*, **121**, 024901.

Asgari G, Seidmohammadi A, Salari M, Ramavandi B. J. Faradmal, (2020). Catalytic ozonation assisted by rGO/C-MgO in the degradation of humic acid from aqueous solution: modeling and optimization by response surface methodology, kinetic study. *Desalination and Water Treatment*, **174**, 215–229.

Guo T, Bulin C. (2021). Facile preparation of MgO/graphene oxide nanocomposite for efficient removal of aqueous Congo red: adsorption performance and interaction mechanism. Research on Chemical Intermediates, **47**, 945–971.

Gusain R, Gupta K, Joshi P, Khatri OP. (2019). Adsorptive removal and photocatalytic degradation of organic pollutants using metal oxides and their composites: A comprehensive review. Advances in Colloid and Interface Science, **272**, 102009.

Kannan K, Hemavathi B, Radhika D, Manjunath H.R, Kumar K, Lakkaboyana S.K, Kakarla R.R, Anjanapura V.R. (2024). Facile synthesis of novel ZnO-MgO nanohybrids and its photocatalytic degradation of toxic pollutants, **317**, 100125

Kant R, Sharma T, Bhardwaj S, Kumar S. (2022). Structural, electrical and optical properties of MgO-reduced graphene oxide nanocomposite for optoelectronic applications. Current Applied Physics, **36**, 76-82

Lin T.H, An H, Nam N.T.H, Hai N.D, Binh T.L, Cong C.Q, Trinh L.N.T, Huy N.L.H, Buu T.T, Minh D.T.C, Phong M.T, Hieu N.H. (2023). Magnesium ferrite/titanium dioxide/reduced graphene oxide composite photocatalyst for degradation of crystal violet under ultraviolet irradiation. *Materials Chemistry and Physics*, **301**, 127661.

Meher-Un-Nisa K, Ahmed N.N, Mehdi M, Thebo K.H, Mahar N, Ayaz Ali M, Memon N, Hussain N. (2023). Synthesis of novel visible light driven MgO@GO nanocomposite photocatalyst for degradation of Rhodamine 6G. Optical Materials,**135**, 113260.

Mohamed A, Mahanna H, Samy M. (2024). Synergistic effects of photocatalysis-periodate activation system for the degradation of emerging pollutants using GO/MgO nanohybrid. *Journal of Environmental Chemical Engineering*, **12**, 112248.

Nagi M, El-Shafai, Amr M.B, Mohamed M, Mohamed S, Ibrahim E. (2021). Enhancement of the photocurrent and electrochemical properties of the modified nanohybrid composite membrane of cellulose/graphene oxide with magnesium oxide nanoparticle (GO@CMC.MgO) for photocatalytic antifouling and supercapacitors applications. Electrochimica *Acta*, **392**, 138989

Sharmin D, Chandra R, Basith, M.A. (2021). Photocatalytic water splitting ability of Fe/MgO-rGO nanocomposites towards hydrogen evolution. *International Journal of Hydrogen Energy*, **46**, 38232-38246

Shuai C, Wang B, Bin S, Peng S, Gao C**.** (2020). Interfacial strengthening by reduced graphene oxide coated with MgO in biodegradable Mg composites. *Materials & Design*, **191**, 108612.

Wang H, Li G, Ali F.J. (2020). Fabrication and structural of the Ag_2S-MgO/graphene oxide nanocomposites with high photocatalysis and antimicrobial activities. *Journal of Photochemistry and Photobiology B: Biology*. **207**, 111882

Wu H, Zhao X, Wang L. (2018). Preparation and surface modification of magnesium hydroxide in a cetyltrimethyl ammonium bromide/isopropanol/cyclohexane/water microemulsion. *Micro Nano Letters*, **13**, 1642–1645.

Yadav P, Saini R, Bhaduri A. (2023). Facile synthesis of MgO nanoparticles for effective degradation of organic dyes. *Environmental Science and Pollution Research*, **30**, 71439–71453.

Yousefi R, Azimi H.R, Mahmoudian M.R, Cheraghizade M. (2018). Highly enhanced photocatalytic performance of Zn(1−x)MgxO/rGO nanostars under sunlight irradiation synthesized by one-pot refluxing method. *Advanced Powder Technology*, **129**, 78-85

Zen W, Gao M, Liu K, Li C, Cao N, Zhao X, Wei T. (2021). Boosting charge separation and surface defects for superb photocatalytic activity of magnesium oxide/graphene nanosheets. *Applied Surface Science,* **535**, 147658

Zheng Y, Cao L, Xing G. (2019). Microscale flower-like magnesium oxide for highly efficient photocatalytic degradation of organic dyes in aqueous solution. *RSC Advances*, **9**, 7338–7348

Zhou W, Upreti S, Whittingham M.S. (2011). High performance Si/MgO/graphite composite as the anode for lithium-ion batteries. *Electrochemistry Communications*, **13**, 1102-1104.